PCCP

PAPER

View Article Online
View Journal | View Issue



Cite this: *Phys. Chem. Chem. Phys.*, 2024, **26**, 28980

# Electronic relaxation pathways in thio-acridone and thio-coumarin: two heavy-atom-free photosensitizers absorbing visible light†

Chris Acquah, [a] Sean Hoehn, [a] Sarah Krul, [a] Steffen Jockusch, [b] Shudan Yang, [c] Sourav Kanti Seth, [a] Eric Lee, [a] Han Xiao [cdef] and Carlos E. Crespo-Hernández *[a]

Received 26th September 2024,
Accepted 9th November 2024

DOI: 10.1039/d4cp03720k

rsc.li/pccp

Heavy-atom-free photosensitizers (HAF-PSs) have emerged as a new class of photosensitizers aiming to broaden their applicability and versatility across various fields of the photodynamic therapy of cancers. The strategy involves replacing the exocyclic oxygen atoms of the carbonyl groups of established biocompatible organic fluorophores with sulfur, thereby bathochromically shifting their absorption spectra and enhancing their intersystem crossing efficiencies. Despite these advancements, the photophysical attributes and electronic relaxation mechanisms of many of these HAF-PSs remain inadequately elucidated. In this study, we investigate the excited state dynamics and photochemical properties of two promising HAF-PSs, thio-coumarin and thio-acridone. Employing a combination of steady-state and time-resolved techniques from femtoseconds to microseconds, coupled with quantum chemical calculations, we unravel the electronic relaxation mechanisms that give rise to the efficient population of long-lived and reactive triplet states in these HAF-PSs.



## Introduction

Heavy-atom-free photosensitizers (HAF-PSs), derived from the thionation of carbonyl groups in readily accessible organic fluorophores, are rapidly emerging as a versatile class of compounds.[1–12] This oxygen by sulfur substitution significantly alters the photophysical and photochemical properties of the organic fluorophores. Thionation drastically reduces the emission of fluorophores due to various factors. Particularly in HAF-PSs, the $S_1$ state predominantly has nπ* character with minimal oscillator strength. Furthermore, the efficient intersystem crossing (ISC) between the singlet and triplet states, along with large spin–orbit coupling elements between them, notably reduces the likelihood of fluorescence, as evidenced by their negligible fluorescence quantum yields (FLQY).[3,13,14] Furthermore, thionation causes a redshift in the absorption spectra of standard organic fluorophores into the visible and near-infrared range (400–800 nm), thereby transforming them into exceptional photodynamic therapy chromophores in the therapeutic window and enabling their selective photoactivation.[1–3,13–15]

The remarkable properties imparted by thionation have paved the way for the development of novel HAF-PSs, boasting superior photochemical characteristics compared to their halogen[16] and heavy-metal counterparts.[17,18] Several recently developed HAF-PSs exhibit favorable characteristics such as biocompatibility, biodegradability, low dark cytotoxicity, and structural robustness.[1–3,14] Shown in Scheme 1 are two notable HAF-PSs, thionated acridone (SACD) and thionated coumarin (SCou), both exhibiting biocompatibility and minimal cytotoxicity in cancer cells and 3D multicellular tumor spheroids.[3]

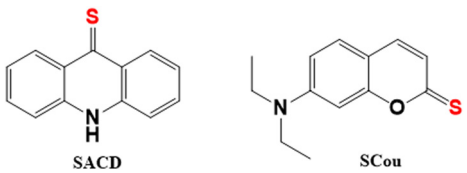


Scheme 1 Molecular structure of thio-acridone (SACD) (left) and thio-coumarin (SCou) (right).

[a] *Department of Chemistry, Case Western Reserve University, Cleveland, OH 44106, USA. E-mail: cxc302@case.edu*
[b] *Center for Photochemical Sciences, Bowling Green State University, Bowling Green, Ohio, 43403, USA*
[c] *Department of Chemistry, Rice University, 6100 Main Street, Houston, Texas, 77005, USA*
[d] *Department of Biosciences, Rice University, 6100 Main Street, Houston, Texas, 77005, USA*
[e] *Department of Bioengineering, Rice University, 6100 Main Street, Houston, Texas, 77005, USA*
[f] *SynthX Center, Rice University, 6100 Main Street, Houston, Texas, 77005, USA*
† Electronic supplementary information (ESI) available. See DOI: https://doi.org/10.1039/d4cp03720k

However, their electronic relaxation mechanisms leading to the efficient population of the long-lived and reactive triplet state have not been elucidated. Understanding these mechanisms is crucial for advancing the development of HAF-PSs for applications in photodynamic therapy, photovoltaics, and photon-upconversion.

In this contribution, we investigate the excited-state dynamics of SACD and SCou in acetonitrile (ACN) and dimethyl sulfoxide (DMSO) solvents. We employ a combination of steady-state absorption, emission, femtosecond broadband transient absorption, and nanosecond laser flash photolysis measurements, along with quantum chemical calculations to elucidate their electronic relaxation pathways upon excitation with visible light at 470 nm. As observed for several thiobases[19–23] and HAF-PSs[1–3,14,15] investigated to date, visible light excitation of SACD and SCou leads to high triplet quantum yields and high quantum yields of singlet oxygen ($^1O_2$) generation of 0.93 ± 0.05 and 0.43 ± 0.05, respectively. In addition, both molecules exhibit long-lived triplet states with triplet decay lifetimes of 2.85 ± 0.02 μs and 10.5 ± 0.3 μs in deoxygenated ACN for SACD and SCou, respectively.

## Results and discussion

### Steady-state spectroscopy

Fig. 1 illustrates the steady-state absorption spectra of (a) SACD and (b) SCou in ACN and DMSO. In ACN, SACD displays three distinct absorption bands, with the lowest energy band peaking at 477 nm. In DMSO, this band shifts slightly to 484 nm. Likewise, SCou shows a distinct absorption band with a maximum absorbance at 467 nm in ACN and 475 nm in DMSO, accompanied by two smaller bands spanning the 250 to 375 nm range in both solvents. The absorption spectra of both molecules in DMSO, a solvent characterized by a dielectric constant of 46.7,[24] exhibit a redshift of approximately 5 nm compared to their counterparts in ACN, which has a dielectric constant of 36.0.[24] This redshift likely arises from solvent-induced effects such as polarity, leading to stabilization of the electronic excited states. This observation aligns well with the simulated absorption spectra (Fig. S1, ESI†), obtained using the TD-PBE0-D3BJ/CPCM/def2-TZVPD//B3LYP$_G$-D3BJ/CPCM/def2-TZVPD level of theory for both molecules in ACN and DMSO following optimization of the ground state structures.

Upon excitation at 470 nm, SACD exhibits weak emission with a quantum yield of $<0.001$[3] centred around 645 nm in ACN and approximately 636 nm in DMSO (Fig. 1c). When subjected to $N_2$-saturated conditions, there is a noticeable rise in the intensity of the emission band centred at approximately 645 nm and 636 nm in ACN and DMSO, respectively (Fig. S2a and S3a, ESI†). Consequently, the emission bands at 645 nm and 636 nm are indicative of phosphorescence. Notably, excitation spectra captured at these emission maxima closely align with the steady-state absorption spectra, confirming that the emission is an inherent property of these compounds and not due to impurities (Fig. S2b and S3b, ESI†). Interestingly, SACD exhibited a considerable Stokes shift in both solvents, indicating a large energy difference between the singlet and triplet states.

In contrast, SCou displayed emissions at approximately 524 nm in ACN and 527 nm in DMSO upon excitation at 470 nm (Fig. 1d).

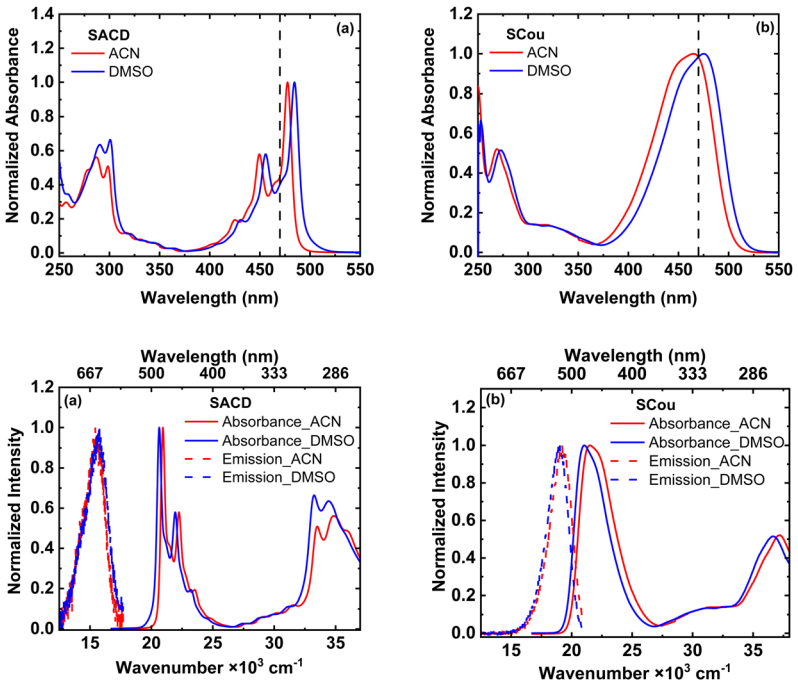


Fig. 1 (Top) Normalized steady-state absorption spectra of (a) SACD and (b) SCou in ACN (red) and DMSO (blue). Vertical dashed lines indicate the excitation wavelength of 470 nm used in the transient and emission experiments. (Below) Comparism of the emission spectra (dashed lines) and absorption spectra (solid lines) of (c) SACD and (d) SCou.

Notably, there were no changes in the emission bands under $N_2$-saturated conditions in both solvents, confirming fluorescence emission (Fig. S4a and c, ESI†). However, excitation spectra captured at the corresponding emission wavelengths exhibit less agreement with the steady-state absorption spectra in either solvent (Fig. S4b and d, ESI†). The calculations reported in the next section suggest that the differences between the excitation and absorption spectra for SCou are associated to the strong coupling of the $^1\pi\pi^*$ and $^1n\pi^*$ states in the Franck–Condon (FC) region of the potential energy surfaces (see below). Collectively, the replacement of carbonyl groups with thiocarbonyl groups leads to substantial quenching of fluorescence emission in both molecules, nearly reducing their quantum yields to zero.

### Quantum chemical calculations

Ground state optimizations for each molecule were conducted using density functional theory (DFT)[25] calculations at the B3LYP$_G$-D3BJ/CPCM/def2-TZVPD level of theory. Subsequently, vertical excitation energies (VEE) were calculated at the TD-PBE0/CPCM/def2-TZVPD level of theory in DMSO and ACN. The PBE0[26] functional was chosen for all time-dependent calculations due to its superior accuracy in modelling the absorption of the molecules compared to other functionals tested, such as CAM-B3LYP[27] and X3LYP[28] (Tables S1–S4, ESI†). Tables 1 and 2 present the energies and the oscillator strengths for the three lowest singlet and four lowest triplet states of SACD and SCou in both solvents. Additionally, the percent contributions of the single electron transitions and the Kohn–Sham orbitals for both molecules are illustrated in Tables S5–S8 and Fig. S5–S8 (ESI†) respectively.

Based on the findings outlined in Table 1, it is predicted that SACD predominantly populates its second lowest energy $S_2(\pi\pi^*)$ state upon excitation at 470 nm (2.64 eV) in both solvents. This assertion stems from the observation that the lowest energy singlet state ($S_1$) primarily exhibits an $n\pi^*$ character with minimal oscillator strength, supporting its nonfluorescent nature. Moreover, given the presence of three triplet states at lower energies than the $S_2$ state, it is possible that ISC to the triplet manifold could compete with nonradiative decay to the ground state. Hence, following the optimization of the $S_1$ and $S_2$ excited states, the optimized structures were used to calculate spin–orbit coupling constants (SOCs) between the relevant singlet and triplet states for both molecules in ACN and DMSO (Table 2). These computations were carried out using the TD-PBE0-D3BJ/CPCM/def2-TZVPD//B3LYP$_G$-D3BJ/CPCM/def2-TZVPD level of theory. Considering the computed SOC values and the

Table 1 Vertical excitation energies (eV), oscillator strength, and energy gaps (eV) between relevant singlet and triplet excited states using the optimized Franck–Condon (FC) geometry for SACD computed at the TD-PBE0-D3BJ/CPCM/def2-TZVPD//B3LYP$_G$-D3BJ/CPCM/def2-TZVPD level of theory in ACN and DMSO

| ACN | | | | DMSO | | | |
|---|---|---|---|---|---|---|---|
| State | Electronic character | Energy (eV) | Oscillator strength | State | Electronic character | Energy (eV) | Oscillator strength |
| $S_1$ | $n\pi^*$ | 2.39 | 0.00 | $S_1$ | $n\pi^*$ | 2.39 | 0.00 |
| $S_2$ | $\pi\pi^*$ | 3.12 | 0.34 | $S_2$ | $\pi\pi^*$ | 3.09 | 0.37 |
| $S_3$ | $\pi\pi^*$ | 3.81 | 0.05 | $S_3$ | $\pi\pi^*$ | 3.79 | 0.05 |
| $T_1$ | $\pi\pi^*$ | 1.99 | | $T_1$ | $\pi\pi^*$ | 1.99 | |
| $T_2$ | $n\pi^*$ | 2.15 | | $T_2$ | $n\pi^*$ | 2.16 | |
| $T_3$ | $\pi\pi^*$ | 2.84 | | $T_3$ | $\pi\pi^*$ | 2.84 | |
| $T_4$ | $\pi\pi^*$ | 3.44 | | $T_4$ | $\pi\pi^*$ | 3.44 | |
| $\Delta E(S_1–T_1)$ | | 0.39 | | $\Delta E(S_1–T_1)$ | | 0.39 | |
| $\Delta E(S_1–T_3)$ | | −0.46 | | $\Delta E(S_1–T_3)$ | | −0.46 | |
| $\Delta E(S_1–T_4)$ | | −1.05 | | $\Delta E(S_1–T_4)$ | | −1.05 | |
| $\Delta E(S_2–T_2)$ | | 0.97 | | $\Delta E(S_2–T_2)$ | | 0.93 | |
| $\Delta E(S_3–T_2)$ | | 1.66 | | $\Delta E(S_3–T_2)$ | | 1.64 | |

Table 2 Calculated spin–orbit couplings constants for SACD in DMSO and ACN computed at the TD-PBE0-D3BJ/CPCM/def2-TZVPD//B3LYP$_G$-D3BJ/CPCM/def2-TZVPD level of theory using the FC, $S_1$ and $S_2$ minimum geometries

| FC geometry | SOC ($cm^{-1}$) | $S_1$ minimum | SOC ($cm^{-1}$) | $S_2$ minimum | SOC ($cm^{-1}$) |
|---|---|---|---|---|---|
| ACN | | | | | |
| $S_1–T_1(^1n\pi^*–^3\pi\pi^*)$ | 115 | $S_1–T_1(^1n\pi^*–^3\pi\pi^*)$ | 124 | $S_1–T_1(^1n\pi^*–^3\pi\pi^*)$ | 115 |
| $S_1–T_3(^1n\pi^*–^3\pi\pi^*)$ | 82 | $S_1–T_3(^1n\pi^*–^3\pi\pi^*)$ | 77 | $S_1–T_3(^1n\pi^*–^3\pi\pi^*)$ | 87 |
| $S_1–T_4(^1n\pi^*–^3\pi\pi^*)$ | 0.2 | $S_1–T_4(^1n\pi^*–^3\pi\pi^*)$ | 0.6 | $S_1–T_4(^1n\pi^*–^3\pi\pi^*)$ | 0.6 |
| $S_2–T_2(^1\pi\pi^*–^3n\pi^*)$ | 96 | $S_2–T_2(^1\pi\pi^*–^3n\pi^*)$ | 111 | $S_2–T_2(^1\pi\pi^*–^3n\pi^*)$ | 98 |
| $S_3–T_2(^1\pi\pi^*–^3n\pi^*)$ | 100 | $S_3–T_2(^1\pi\pi^*–^3n\pi^*)$ | 93 | $S_3–T_2(^1\pi\pi^*–^3n\pi^*)$ | 104 |
| DMSO | | | | | |
| $S_1–T_1(^1n\pi^*–^3\pi\pi^*)$ | 114 | $S_1–T_1(^1n\pi^*–^3\pi\pi^*)$ | 123 | $S_1–T_1(^1n\pi^*–^3\pi\pi^*)$ | 115 |
| $S_1–T_3(^1n\pi^*–^3\pi\pi^*)$ | 82 | $S_1–T_3(^1n\pi^*–^3\pi\pi^*)$ | 77 | $S_1–T_3(^1n\pi^*–^3\pi\pi^*)$ | 87 |
| $S_1–T_4(^1n\pi^*–^3\pi\pi^*)$ | 0.4 | $S_1–T_4(^1n\pi^*–^3\pi\pi^*)$ | 0.6 | $S_1–T_4(^1n\pi^*–^3\pi\pi^*)$ | 0.7 |
| $S_2–T_2(^1\pi\pi^*–^3n\pi^*)$ | 98 | $S_2–T_2(^1\pi\pi^*–^3n\pi^*)$ | 113 | $S_2–T_2(^1\pi\pi^*–^3n\pi^*)$ | 100 |
| $S_3–T_2(^1\pi\pi^*–^3n\pi^*)$ | 98 | $S_3–T_2(^1\pi\pi^*–^3n\pi^*)$ | 92 | $S_3–T_2(^1\pi\pi^*–^3n\pi^*)$ | 102 |

 

El-Sayed's propensity rules,[29] several pathways for ISC to the triplet manifold are predicted to play a role. In SACD, the calculations indicate that ISC is probable between the $S_1 \rightarrow T_1$, $S_1 \rightarrow T_3$ and $S_2 \rightarrow T_2$ transitions in both solvents.

Referring to Table 3, the predominant character of the lowest energy singlet excited state $S_1$ in SCou is $\pi\pi^*$ in DMSO, which is isoenergetic with the $S_2(n\pi^*)$ electronic state. However, this trend reverses in ACN, where the lowest energy singlet state $S_1$ exhibits an $n\pi^*$ character, also isoenergetic with the $S_2(\pi\pi^*)$ state. Given the characteristic $\pm 0.3$ eV error associated with TD-DFT calculations,[14,25,30] both $^1\pi\pi^*$ and $^1n\pi^*$ states are predicted to be practically isoenergetic and strongly coupled in the FC region of the potential energy surfaces in both solvents. As noted above, the strong coupling between the $^1\pi\pi^*$ and $^1n\pi^*$ states in the FC region could explain the experimentally observed differences between the absorption and excitation spectra of SCou in both solvents. Considering the negligible oscillator strength usually associated with $n\pi^*$ transitions, it is expected that most of the excited state population would initially reside in the $^1\pi\pi^*$ state after excitation at 470 nm in both solvents. Furthermore, with three triplet states positioned lower in energy than the $^1\pi\pi^*$ state, ISC to the triplet manifold is likely to be competitive in both solvents. Hence, together with the optimized ground state geometry, the optimized $^1\pi\pi^*$ and $^1n\pi^*$ structures of SCou were used to compute SOCs between the relevant singlet and triplet states for both molecules in ACN and DMSO (Table 4). This analysis was conducted using the TD-PBE0-D3BJ/CPCM/def2-TZVPD//B3LYP$_G$-D3BJ/CPCM/def2-TZVPD level of theory.

According to the results presented in Table 4, effective ISC in SCou are anticipated between the $S_1$ state and the $T_1$ and $T_3$ states, and between the $S_2$, $S_3$ states with the $T_2$ state in ACN. In DMSO, efficient ISC are predicted between the $S_2$ state and the $T_1$ and $T_3$ states, and between the $S_1$, $S_3$ states with the $T_2$ state. This is supported by the observation that both the $S_1$ and $S_2$ states of SCou in both solvents possess an isoenergetic alignment with the $T_3(\pi\pi^*)$ state, suggesting a strong coupling between these states in the FC region, thereby facilitating efficient ISC to the triplet manifold. The diverse ISC pathways predicted above for both compounds underscore the pivotal role of thionation in enhancing ISC to the triplet manifold in these HAF-PSs.

### Excited state optimizations

The mechanism of electronic relaxation, as indicated by the VEE at the FC geometry discussed above, may involve the participation of multiple excited electronic states. To explore this possibility further, the nuclear coordinates for the $S_1$, $S_2$,

Table 3 Vertical excitation energies (eV), oscillator strength, and energy gaps (eV) between relevant singlet and triplet excited states using the optimized FC-geometry for SCou computed at the TD-PBE0-D3BJ/CPCM/def2-TZVPD//B3LYP$_G$-D3BJ/CPCM/def2-TZVPD level of theory in ACN and DMSO

| ACN | | | | DMSO | | | |
|---|---|---|---|---|---|---|---|
| State | Electronic character | Energy (eV) | Oscillator strength | State | Electronic character | Energy (eV) | Oscillator strength |
| $S_1$ | $n\pi^*$ | 3.08 | 0.01 | $S_1$ | $\pi\pi^*$ | 3.05 | 0.85 |
| $S_2$ | $\pi\pi^*$ | 3.09 | 0.80 | $S_2$ | $n\pi^*$ | 3.09 | 0.00 |
| $S_3$ | $\pi\pi^*$ | 4.09 | 0.17 | $S_3$ | $\pi\pi^*$ | 4.01 | 0.17 |
| $T_1$ | $\pi\pi^*$ | 2.06 | | $T_1$ | $\pi\pi^*$ | 2.06 | |
| $T_2$ | $n\pi^*$ | 2.84 | | $T_2$ | $n\pi^*$ | 2.85 | |
| $T_3$ | $\pi\pi^*$ | 3.02 | | $T_3$ | $\pi\pi^*$ | 3.02 | |
| $T_4$ | $\pi\pi^*$ | 3.59 | | $T_4$ | $\pi\pi^*$ | 3.59 | |
| $\Delta E(S_1-T_1)$ | | 1.02 | | $\Delta E(S_2-T_1)$ | | 1.02 | |
| $\Delta E(S_1-T_3)$ | | 0.06 | | $\Delta E(S_2-T_3)$ | | 0.06 | |
| $\Delta E(S_1-T_4)$ | | −0.51 | | $\Delta E(S_2-T_4)$ | | −0.51 | |
| $\Delta E(S_2-T_2)$ | | 0.25 | | $\Delta E(S_1-T_2)$ | | 0.20 | |
| $\Delta E(S_3-T_2)$ | | 1.25 | | $\Delta E(S_3-T_2)$ | | 1.16 | |

Table 4 Calculated spin–orbit couplings constants for SCou in ACN and DMSO computed at the TD-PBE0-D3BJ/CPCM/def2-TZVPD//B3LYP$_G$-D3BJ/CPCM/def2-TZVPD level of theory using the FC, $S_1$ and $S_2$ minimum geometries

| FC geometry | SOC ($cm^{-1}$) | $S_1$ minimum | SOC ($cm^{-1}$) | $S_2$ minimum | SOC ($cm^{-1}$) |
|---|---|---|---|---|---|
| ACN | | | | | |
| $S_1$–$T_1(^1n\pi^*$–$^3\pi\pi^*)$ | 91 | $S_1$–$T_1(^1n\pi^*$–$^3\pi\pi^*)$ | 87 | $S_1$–$T_1(^1n\pi^*$–$^3\pi\pi^*)$ | 103 |
| $S_1$–$T_3(^1n\pi^*$–$^3\pi\pi^*)$ | 99 | $S_1$–$T_3(^1n\pi^*$–$^3\pi\pi^*)$ | 93 | $S_1$–$T_3(^1n\pi^*$–$^3\pi\pi^*)$ | 100 |
| $S_1$–$T_4(^1n\pi^*$–$^3\pi\pi^*)$ | 24 | $S_1$–$T_4(^1n\pi^*$–$^3\pi\pi^*)$ | 22 | $S_1$–$T_4(^1n\pi^*$–$^3\pi\pi^*)$ | 20 |
| $S_2$–$T_2(^1\pi\pi^*$–$^3n\pi^*)$ | 69 | $S_2$–$T_2(^1\pi\pi^*$–$^3n\pi^*)$ | 65 | $S_2$–$T_2(^1\pi\pi^*$–$^3n\pi^*)$ | 84 |
| $S_3$–$T_2(^1\pi\pi^*$–$^3n\pi^*)$ | 93 | $S_3$–$T_2(^1\pi\pi^*$–$^3n\pi^*)$ | 96 | $S_3$–$T_2(^1\pi\pi^*$–$^3n\pi^*)$ | 100 |
| DMSO | | | | | |
| $S_2$–$T_1(^1n\pi^*$–$^3\pi\pi^*)$ | 91 | $S_1$–$T_2(^1\pi\pi^*$–$^3n\pi^*)$ | 70 | $S_1$–$T_1(^1n\pi^*$–$^3\pi\pi^*)$ | 103 |
| $S_2$–$T_3(^1n\pi^*$–$^3\pi\pi^*)$ | 100 | $S_2$–$T_1(^1n\pi^*$–$^3\pi\pi^*)$ | 90 | $S_1$–$T_3(^1n\pi^*$–$^3\pi\pi^*)$ | 100 |
| $S_2$–$T_4(^1n\pi^*$–$^3\pi\pi^*)$ | 23 | $S_2$–$T_3(^1n\pi^*$–$^3\pi\pi^*)$ | 96 | $S_1$–$T_4(^1n\pi^*$–$^3\pi\pi^*)$ | 20 |
| $S_1$–$T_2(^1\pi\pi^*$–$^3n\pi^*)$ | 72 | $S_2$–$T_4(^1n\pi^*$–$^3\pi\pi^*)$ | 23 | $S_2$–$T_2(^1\pi\pi^*$–$^3n\pi^*)$ | 86 |
| $S_3$–$T_2(^1\pi\pi^*$–$^3n\pi^*)$ | 94 | $S_3$–$T_2(^1\pi\pi^*$–$^3n\pi^*)$ | 96 | $S_3$–$T_2(^1\pi\pi^*$–$^3n\pi^*)$ | 100 |

and $T_1$ excited states of both SACD and SCou were optimized in ACN and DMSO at the TD-PBE0/CPCM/def2-TZVPD level of theory. The optimized geometries of the excited states are depicted in Fig. 3 and 4 for SACD and SCou, respectively.

In SACD, the minimum energy structures of the $S_1$, $S_2$, and $T_1$ states in both solvents predominantly exhibit planar structures with minimal conformational changes (Fig. 2a and b). A notable structural variation involves changes in the bond length of the carbon–sulfur bond. In ACN, the bond lengths measure 1.690 (1.691), 1.727 (1.726), 1.713 (1.713), 1.712 (1.712) angstrom for $S_0$, $S_1$, $S_2$, and $T_1$, respectively, with corresponding values in parentheses for DMSO (Fig. 2c).

Similarly, in SCou, the minimum energy structures of $S_1$, $S_2$, and $T_1$ states in both solvents generally exhibit planarity, except for the diethyl in the *N*,*N*-diethylamino functional group, which is out of plane (Fig. 3a and b). There are also significant structural differences highlighted by variations in the bond length of the carbon–sulfur bond. In ACN, the bond lengths are as follows: 1.673 (1.673), 1.689 (1.689), 1.734 (1.734), 1.683 (1.683) angstrom for $S_0$, $S_1$, $S_2$, and $T_1$ respectively, with corresponding values in parentheses representing optimizations in DMSO (Fig. 3c).

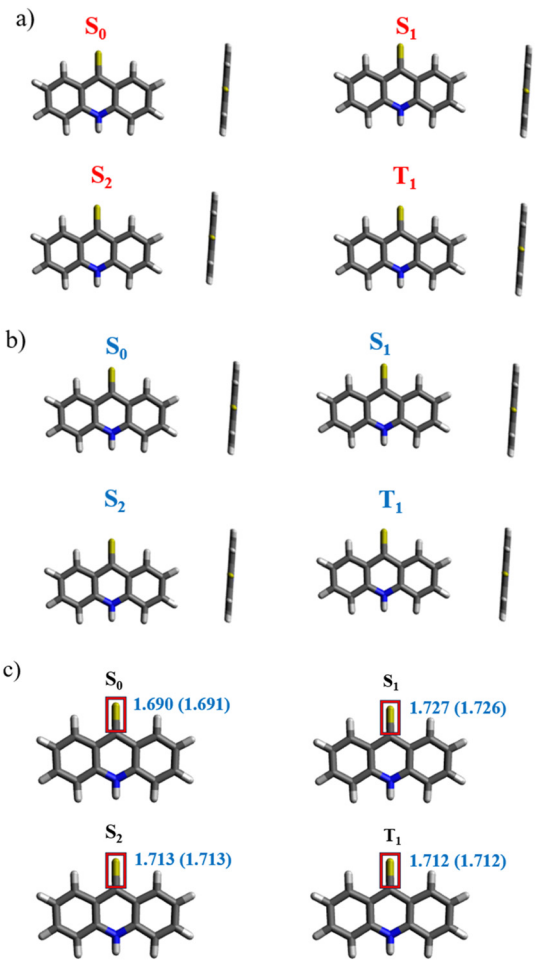


Fig. 2 Optimized geometries of relevant excited states for SACD at the TD-PBE0/CPCM/def2-TZVPD level of theory in (a) ACN and (b) DMSO. (c) The important bond length changes for the relevant excited state geometries for SACD in ACN. The bond length values are in Angstrom and values in the parentheses are for DMSO.

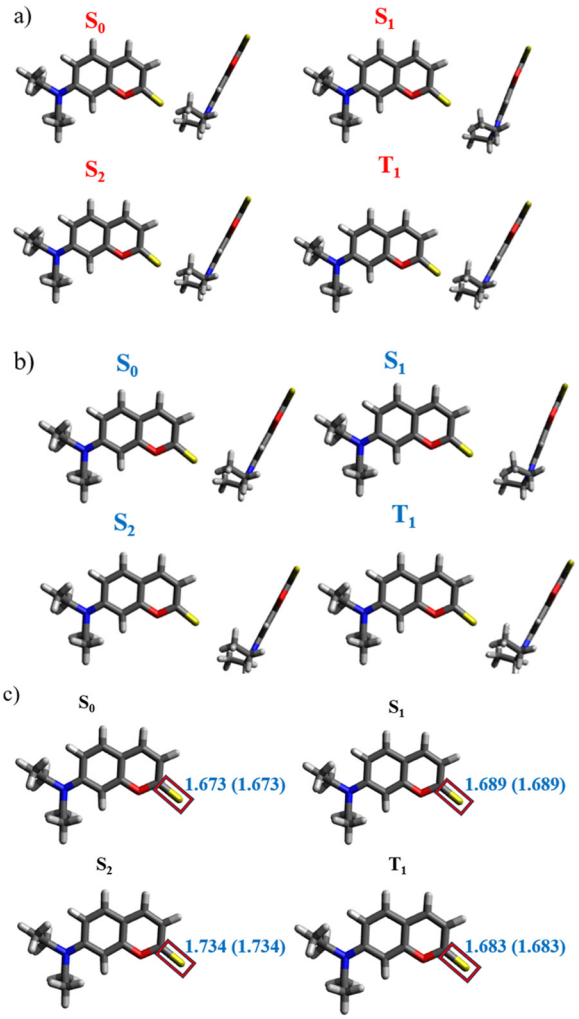


Fig. 3 Optimized geometries of relevant excited states for SCou at the TD-PBE0/CPCM/def2-TZVPD level of theory in (a) ACN and (b) DMSO. (c) The important bond length changes for the relevant excited state geometries for SACD in ACN. The bond length values are in Angstrom and values in the parentheses are for DMSO.

Additionally, the emission properties were examined using TD-DFT by optimizing the $S_1$, $S_2$ and $T_1$ structures. For SACD, the vertical $T_1 \rightarrow S_0$ emission wavelength is predicted to occur around 652 nm. This theoretical prediction closely matches the observed experimental emissions of 645 nm in ACN and 636 nm in DMSO. For SCou, the predicted vertical $S_1 \rightarrow S_0$ or $S_2 \rightarrow S_0$ emission wavelength are 477 nm and 476 nm, respectively. These predictions correspond well with the observed experimental emissions of 523 nm in ACN and 527 nm in DMSO. Furthermore, the excitation energy of the $^1\pi\pi^*$ state (*i.e.*, the $E_{0,0}$) for SCou is estimated to be 2.93 eV in both solvents. These predicted values are in good agreement with the experimentally obtained values of 2.53 eV in ACN and 2.48 eV in DMSO.

 

While SACD and SCou exhibit negligible fluorescence quantum yields (<0.001),[3] their oxygen congeners, coumarin (Cou) and acridone (ACD) exhibit large emission quantum yields of 71% and 64%.[3] Hence, and for completeness, we performed ground state optimizations for Cou and ACD at the B3LYP$_G$-D3BJ/CPCM/def2-TZVPD level of theory, followed by calculating the VEE and SOC values at the TD-PBE0/CPCM/def2-TZVPD level of theory in DMSO and ACN. The VEEs and SOCs of ACD and Cou using the FC geometry are reported in Tables S11–S16 (ESI†), respectively. The lowest energy excited singlet state ($S_1$) of ACD in both solvents exhibits a ππ* character. El-Sayed's propensity rules suggest that ISC to the triplet manifold may occur between the $S_1(\pi\pi^*)$ state and the $T_2(n\pi^*)$ state and between the $S_2(n\pi^*)$ and $T_1(\pi\pi^*)$ states. Other possible ISC routes like $S_2 \rightarrow T_3$ and $S_3 \rightarrow T_2$ show small SOC values, as indicated in Table S15 (ESI†). For Cou, the three lowest singlet and triplet states display a ππ* character in both solvents, implying an unfavorable ISC to the triplet manifold based on El-Sayed's rules and the computed small SOC values (Table S16, ESI†). The results from these calculations predict that a low yield of $T_1$ state population (<29%) may occur in ACD, while most of the 34% nonradiative decay in Cou is expected to occur through internal conversion to the ground state.

### Femtosecond broadband transient absorption spectroscopy

The investigation of the excited state dynamics of SACD and SCou involved the analysis of time-resolved absorption spectra. Fig. 4 display the transient absorption spectra for SACD upon 470 nm excitation in ACN and DMSO, while Fig. 5 shows the representative decay traces with best fits and evolution-associated difference spectra. Similar data are presented in Fig. 7 and 8 for SCou. Table 5 presents the lifetimes obtained from a globally fit analysis of the transient data of SACD and SCou using a three or four-component sequential model, respectively. Despite the general similarities in the transient absorption spectra for both molecules in both solvents, a few noteworthy distinctions are detailed in Fig. 4.

The broadband transient absorption spectra of SACD in ACN are shown in Fig. 4a. In the first panel (Fig. 4a–i), within the cross-correlation of the pump and probe beams, three positive $\Delta A$ maxima are observed at 415 nm, 527 nm, and 650 nm, while four negative $\Delta A$ bands can be seen within the 424 nm to 560 nm range, with the highest intensity band having a maximum at 477 nm. In the second panel (Fig. 4a–ii), within the following *ca.* 1 ps, the transient species absorbing at 515 nm begins to increase in intensity and slightly blue shift, while simultaneously, the positive band in the far visible region at 650 nm decreases in amplitude. Between *ca.* 1 ps and 33 ps, the initial small positive band at 415 nm decays completely, while the negative band at 515 nm blue shifts and reduces intensity until it forms a new positive band absorbing from 478 nm to 550 nm with a maximum at 525 nm. Notably, an apparent isosbestic point is observed around 478 nm. Lastly (Fig. 4a–iv), from approximately 32 ps, and until the end of our probing regime of 3 ns, minimal changes in the transient absorption spectra are observed, indicating the population of a long-lived species persisting beyond the 3 ns probe window. Representative decay traces, best fits, and evolution-associated difference spectra are shown in Fig. 5a and b.

Similarly, for SACD in DMSO, in the first panel (Fig. 4b-i), two positive $\Delta A$ bands are observed at 418 nm and 660 nm within the cross-correlation of the pump and probe beams, which is accompanied by a third positive band emerging at 537 nm. Meanwhile, four negative $\Delta A$ bands can be seen within

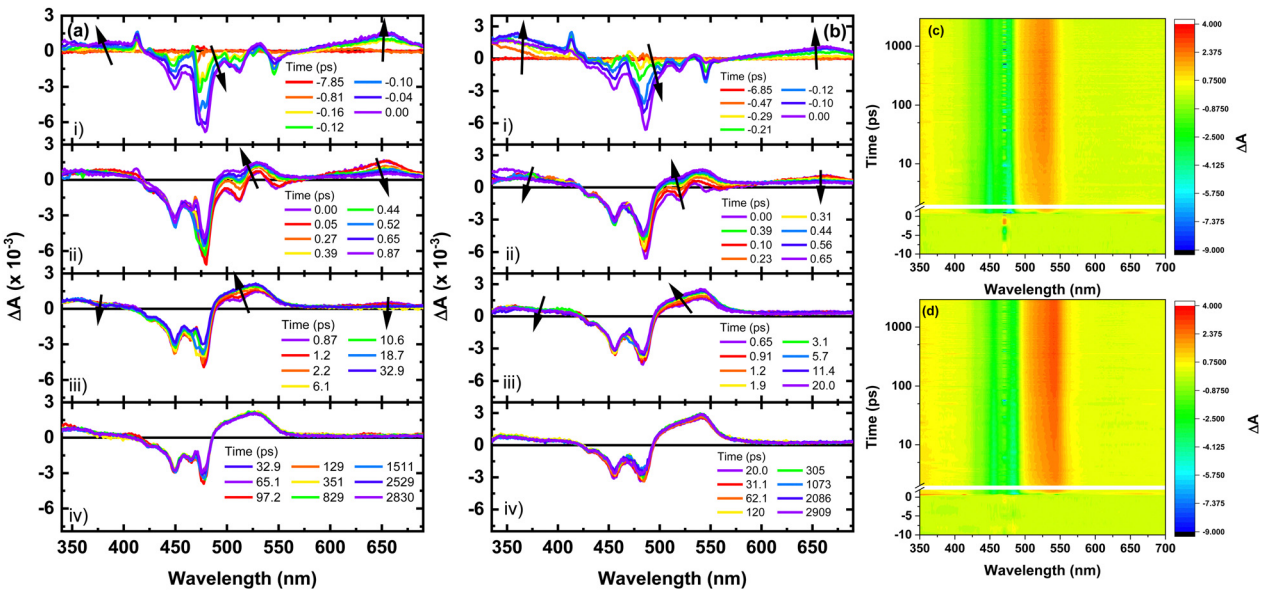


Fig. 4 Spectral evolution of the transient absorption spectra (TAS) of SACD in (a) ACN and (b) DMSO following excitation at 470 nm. The negative spike at *ca.* 413 nm in (a-i), and (b-i) corresponds to the inverse (optical component artifact) of the stimulated Raman emission from the solvent. Representative contour plots of the TAS data for SACD in (c) ACN and (d) DMSO.

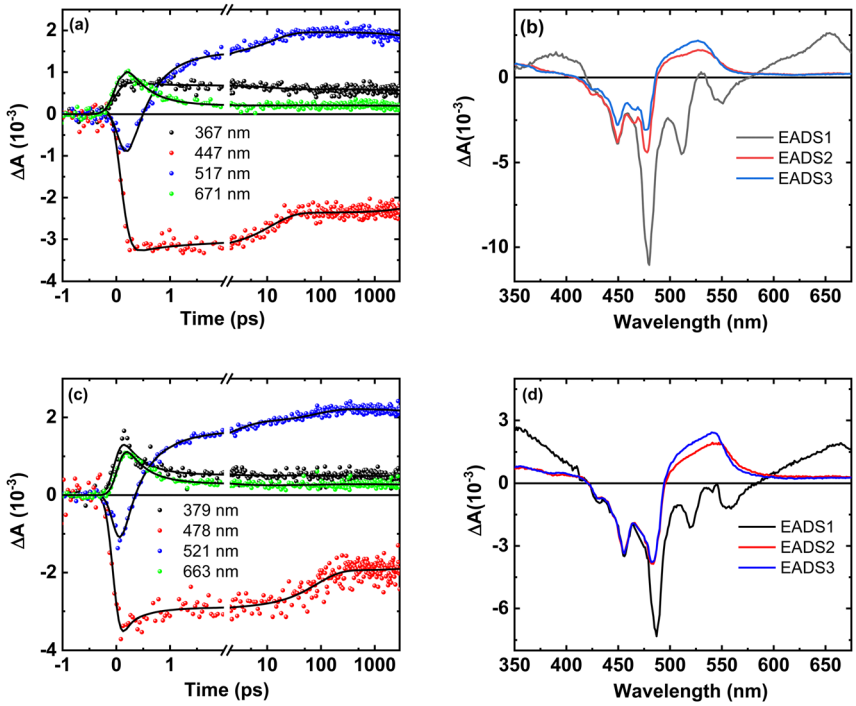


Fig. 5 Representative kinetic decay traces (left) and evolution-associated difference spectra (EADS, right) obtained from global and target analyses of SACD in ACN (a) and (b) and in DMSO (c) and (d). The breaks on the *x*-axis of figure (a) and (c) represent the change in scale from linear to logarithmic.

Table 5 Lifetimes extracted from the transient absorption data for SACD and SCou upon excitation at 470 nm using a globally fit analysis with a three and four-component sequential model, respectively. All errors are reported as twice the standard deviation

| | SACD | | SCou | |
|---|---|---|---|---|
| Lifetime | ACN | DMSO | ACN | DMSO |
| $\tau_1$ | 0.4 ± 0.1 ps | 2.6 ± 0.2 ps | 0.5 ± 0.1 ps | 0.8 ± 0.1 ps |
| $\tau_2$ | 12 ± 1 ps | 84 ± 1 ps | 3.5 ± 0.1 ps | 10.0 ± 0.1 ps |
| $\tau_3$ | >3 ns | >3 ns | 18 ± 1 ps | 106 ± 2 ps |
| $\tau_4$ | — | — | >3 ns | >3 ns |

the 424 nm to 560 nm range with the higher intensity band having a maximum at 485 nm. In the second panel (Fig. 4b-ii), within the following *ca.* 1 ps, the transient species absorbing at 520 nm begins to increase in intensity and slightly blue shift, while simultaneously, the positive band in the far visible region at 660 nm decreases in amplitude. Between *ca.* 1 ps and 33 ps, the initial small positive band at 418 nm decays completely, while the negative band at 519 nm blue shifts and reduces intensity until it forms a new positive Δ*A* band absorbing from 500 nm to 562 nm with a maximum at 540 nm. An apparent isosbestic point is observed around 500 nm. Lastly (Fig. 4b-iv), from approximately 20 ps, and until the end of the probing window of 3 ns, minimal changes in the transient absorption spectra are observed, indicating the population of a long-lived species. Representative decay traces, best fits, and evolution-associated difference spectra are shown in Fig. 5c and d.

The broadband transient absorption spectra of SCou in ACN can be seen in Fig. 6a. In the first panel, (Fig. 6a-i), within the cross-correlation of the pump and probe beams, a positive Δ*A* band maximum is observed at around 425 nm, and a negative Δ*A* band is observed broadly absorbing from *ca.* 440–700 nm with a maximum near 480 nm. Within the following *ca.* 500 fs, the transient species absorbing maximally at 400 nm begins to decay and blue shift, while simultaneously, the absorption throughout the visible region slightly decreases in amplitude (Fig. 6a-ii). As shown in the third panel at probe wavelengths less than 475 nm (Fig. 6a-iii), a blue shift and slight decrease in Δ*A* is observed, whereas in the far visible probing region, the transient species slightly blue shifts and an increase in Δ*A* is observed. An apparent isosbestic point is observed at *ca.* 480 nm. Lastly, in the last panel (Fig. 6a-iv), from approximately 12 ps, and until the end of our probing regime of 3 ns, little changes in the transient absorption spectra are observed, indicating the population of a long-lived species persisting beyond 3 ns.

For SCou in DMSO, in the first panel (Fig. 6b-i), a positive Δ*A* band maximum is observed at around 420 nm and a negative Δ*A* band can be seen broadly stretching from *ca.* 440 to 600 nm with a maximum at 475 nm. At *ca.* 500 fs, the transient species absorbing maximally at 400 nm decays and blue shifts, while also the visible region absorption decreases in amplitude (Fig. 6b-ii). The third panel (Fig. 6b-iii) shows that blue shifting occurs across the broadband spectrum, where a decrease in Δ*A* is observed at probe wavelengths less than 475 nm and an increase in Δ*A* is observed at probe wavelengths longer than 500 nm. An apparent isosbestic point is observed at approximately 500 nm. Finally, from 12 ps,

 

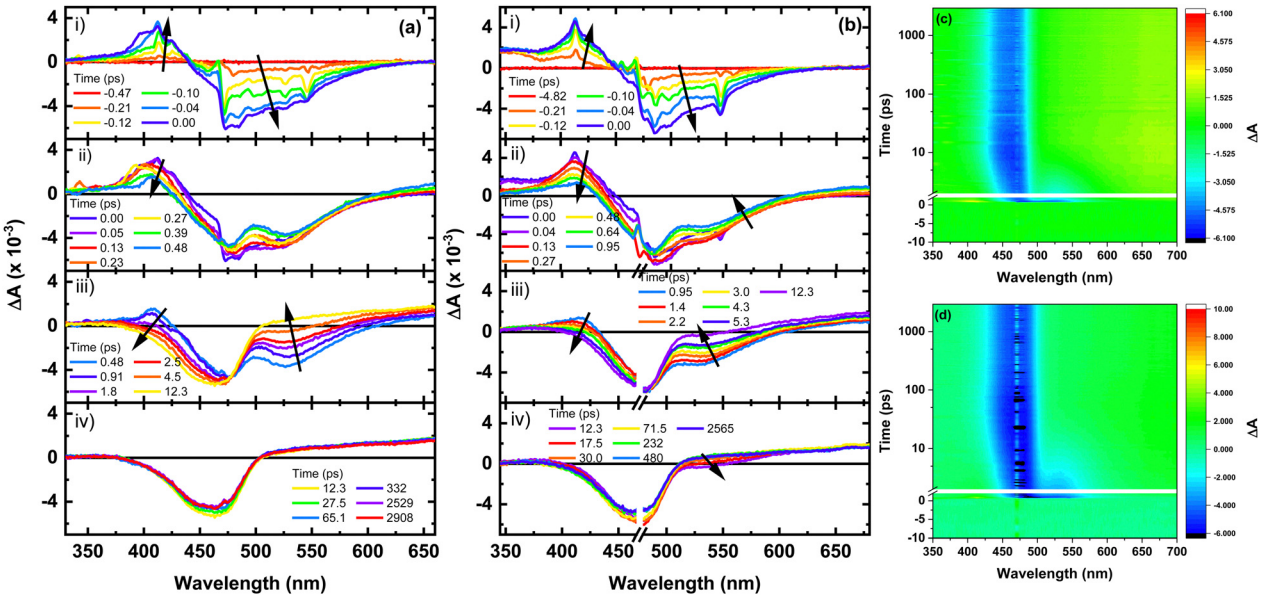


Fig. 6 Spectral evolution of the transient absorption spectra of SCou in (a) ACN and (b) DMSO following excitation at 470 nm. The negative spike at *ca.* 413 nm in (a-i), and (b-i) corresponds to the inverse (optical component artifact) of stimulated Raman emission from the solvent. The breaks in (b) are covering the scattering of the pump reaching the detectors. Representative contour plots of the TAS data for SCou in (c) ACN and (d) DMSO.

and until the end of the probing regime of 3 ns (Fig. 6b-iv), little changes in the transient absorption spectra are observed, which indicates the population of a long-lived species. Representative decay traces, best fits, and evolution-associated difference spectra are shown in Fig. 7c and d.

## Nanosecond laser flash photolysis and singlet oxygen yield experiments

The transient absorption spectra discussed in the preceding sections are limited to a temporal range of 3 ns. To gather essential insights into the kinetics related to the decay of the

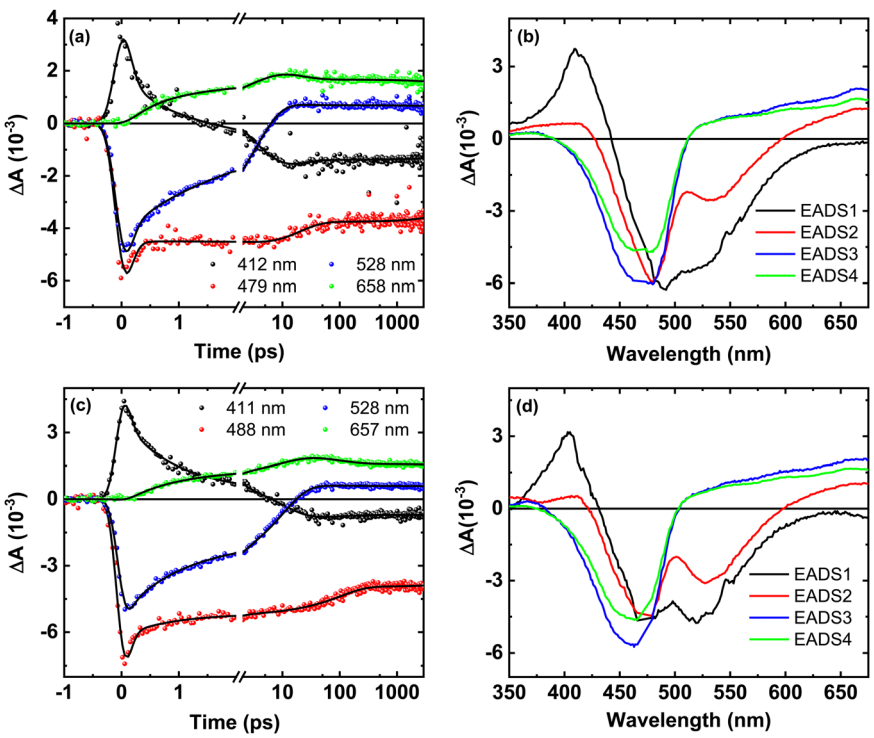


Fig. 7 Representative kinetic decay traces (left) and evolution-associated difference spectra (EADS, right) obtained from global and target analyses of SCou in ACN (a) and (b) and in DMSO (c) and (d). The breaks on the *x*-axis of figure (a) and (c) represent the change in scale from linear to logarithmic.

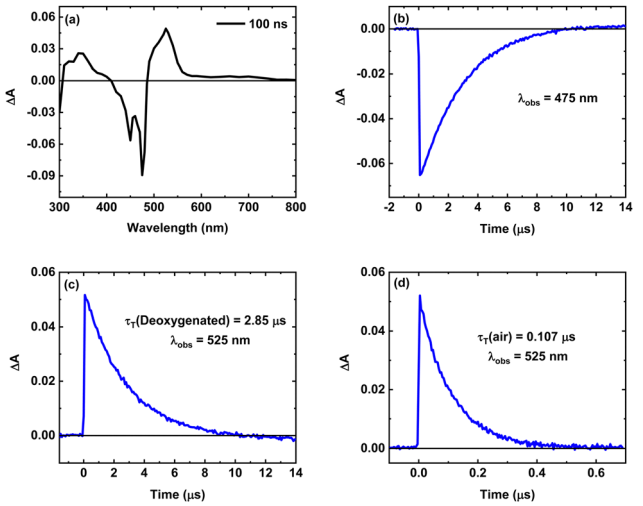


Fig. 8 (a) Transient absorption spectrum of SACD in Ar-saturated acetonitrile solution recorded at a time delay of 100 ns after pulsed laser excitation at 470 nm. (b) Decay trace of the transient absorbance monitored at 475 nm (ground state recovery) in Ar-saturated acetonitrile solution. (c) and (d) Decay traces of the transient absorbance monitored at 525 nm (triplet decay) in Ar-saturated and air-saturated acetonitrile solution.

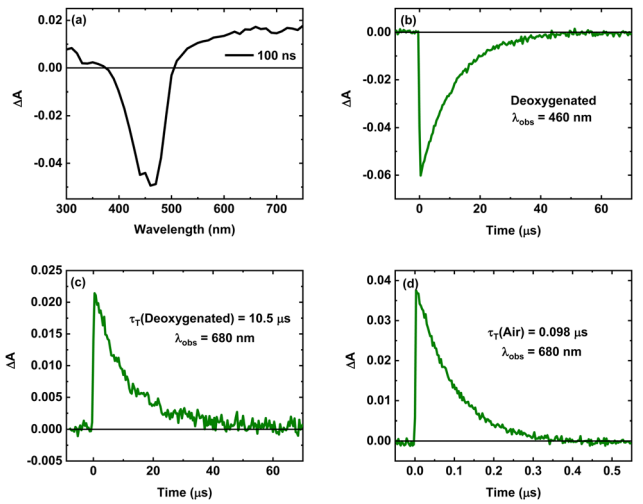


Fig. 9 (a) Transient absorption spectrum of SCou in Ar-saturated acetonitrile solution recorded at a time delay of 100 ns after pulsed laser excitation at 470 nm. (b) Decay trace of the transient absorbance monitored at 460 nm (ground state recovery) in Ar-saturated acetonitrile solution. (c) and (d) Decay traces of the transient absorbance monitored at 680 nm (triplet decay) in Ar-saturated and air-saturated acetonitrile solution.

long-lived species, we used nanosecond laser flash photolysis. As depicted in Fig. 8 and 9, and outlined in Table 6, SACD and SCou display the presence of a long-lived triplet state. In ambient air, the triplet decay lifetimes measured 0.107 ± 0.002 μs for SACD and 0.0980 ± 0.0006 μs for SCou. Under oxygen-saturated conditions, these lifetimes reduced to 0.0230 ± 0.0004 μs and 0.0190 ± 0.0005 μs for SACD and SCou, respectively.

Table 6 Photophysical parameters obtained with nanosecond laser flash photolysis and luminescence techniques for SACD and SCou

| | SACD | SCou |
|---|---|---|
| $\tau_T{}^a$ (μs) | 0.023 ± 0.001 | 0.019 ± 0.001 |
| $\tau_T{}^b$ (μs) | 2.85 ± 0.02 | 10.5 ± 0.3 |
| $\tau_T{}^c$ (μs) | 0.107 ± 0.002 | 0.0980 ± 0.0006 |
| $\Phi\Delta^c$ | 0.93 ± 0.05 | 0.43 ± 0.05 |
| $k_qO_2$ ($10^9$ $M^{-1}$ $s^{-1}$) | 4.7 ± 0.1 | 5.6 ± 0.3 |

[a] $O_2$-saturated. [b] Ar-saturated. [c] Air-saturated.

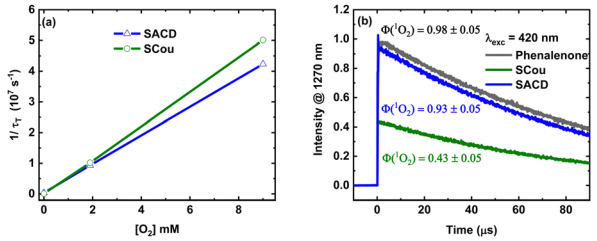


Fig. 10 (a) Determination of the bimolecular triplet quenching constants of SACD and SCou by molecular oxygen. Inverse triplet lifetime *vs.* concentration of molecular oxygen in acetonitrile. (b) Phosphorescence decay traces for singlet oxygen monitored at 1270 nm generated by pulsed photoexcitation at 420 nm of SACD, SCou, or Phenalenone in air-saturated acetonitrile solutions.

Conversely, in argon-saturated conditions, significantly longer lifetimes were observed, measuring 2.85 ± 0.02 μs for SACD and 10.5 ± 0.3 μs for SCou. From lifetimes, the bimolecular triplet quenching rate constants by $O_2$ ($k_qO_2$) were determined for SACD and SCou (Fig. 10a). The $k_qO_2$ values were found to be (4.7 ± 0.1) × $10^9$ and (5.6 ± 0.3) × $10^9$ $M^{-1}$ $s^{-1}$ for SACD and SCou in ACN, respectively (Table 6).

Nanosecond near-infrared emission spectroscopy was also used to measure the singlet oxygen production of SACD and SCou. Fig. 10b illustrates the decay traces of singlet oxygen emission for SACD, SCou, and the phenalenone standard, while Table 6 summarizes the determined quantum yields. Singlet oxygen quantum yields of 0.93 ± 0.05 and 0.43 ± 0.05 were obtained for SACD and SCou in air-saturated conditions in ACN, respectively.

### Electronic relaxation mechanism of SACD in ACN and DMSO

Based on the computational and experimental results outlined in Table 1 and Fig. 4 for SACD, it is expected that the $S_2(\pi\pi^*)$ state should be directly populated in both ACN and DMSO following excitation at 470 nm. Subsequently, a large fraction of the population in the excited $^1\pi\pi^*$ state should undergo ultrafast internal conversion (IC) to the $S_1(n\pi^*)$ state. Considering the substantial SOC values detailed in Table 2 and El-Sayed's rules, it is also expected that ultrafast ISC to the triplet manifold should primarily occur through two competitive pathways. A fraction of the excited $S_2(\pi\pi^*)$ state population should ISC to the $T_2(n\pi^*)$ state, followed by IC to the $T_1(\pi\pi^*)$ state. Another fraction of the $S_2(\pi\pi^*)$ population should IC to the $S_1(n\pi^*)$ state, followed by ISC to the $T_1(\pi\pi^*)$ state. Consequently, we propose

that the first lifetime extracted from the femtosecond transient absorption experiments of approximately *ca.* 0.4 ± 0.01 ps in ACN and 2.6 ± 0.19 ps in DMSO respectively, and the corresponding black EADS, should be assigned to a combination of the $S_2(\pi\pi^*) \rightarrow S_1(n\pi^*) \rightarrow T_1(\pi\pi^*)$ and $S_2(\pi\pi^*) \rightarrow T_2(n\pi^*) \rightarrow T_1(\pi\pi^*)$ pathways. This assignment is supported by the observation of a band peaking at 650 nm in TAS data (Fig. 4a-i), whose decay is accompanied by a net negative change in absorbance ($\Delta A$) at 515 nm (Fig. 4a-ii), and a slight blue shift consistent with the steady-state emission band maxima. The proposed ultrafast ISC to the triplet manifold is also supported by the observation of a low fluorescent quantum yield of $<0.001$.

The decrease in intensity of the negative band at 515 nm (Fig. 4a-iii), leading to the emergence of a new positive band spanning from 478 nm to 550 nm, is attributed to the vibrationally excited $T_1$ states. The negative amplitude band observed between approximately 425 and 500 nm is attributed to ground state depopulation, in agreement with the absorption spectra depicted in Fig. 1a. Hence, the second lifetime, which is associated with the red EADS2 in Fig. 5b–d in both solvents, is attributed to solvent relaxation (SR) and vibrational cooling (VC) within the triplet manifold. The variation of the second lifetime with solvent supports this assignment (*i.e.*, 12 ± 1 ps in ACN and 84 ± 1 ps in DMSO).

The nanosecond transient absorption and the singlet oxygen measurements also support the idea that the triplet population occurs with a near unity yield, considering the measured 93% singlet oxygen quantum yield. The population reaching the $T_1(\pi\pi^*)$ state then decays in 2.85 ± 0.02 μs in Ar-saturated conditions, measured in ACN (Table 6). Hence, we assign the blue EADS3 (Fig. 5b–d) to the $T_1$(min), which is consistent with the calculated excited state absorption spectra (EAS) (Fig. S11, ESI†) for the $T_1$ state. The proposed deactivation mechanism is outlined in Scheme 2a.

### Electronic relaxation mechanism of SCou in ACN and DMSO

According to the calculations, the $^1\pi\pi^*$ and $^1n\pi^*$ states are strongly coupled and practically isoenergetic in both ACN and DMSO. Hence, excitation at 470 nm leads primarily to the population of the $^1\pi\pi^*$ state given its significantly larger oscillator strength. Analysis of the time-resolved absorption data depicted in Fig. 6, reveals a positive change in amplitude in both solvents, peaking around 425 nm. This phenomenon is attributed to the overlap between the initially excited $^1\pi\pi^*$state and $^1n\pi^*$ state in both solvents. Moreover, the broad negative $\Delta A$ band observed between approximately 400 nm to 500 nm in both solvents (Fig. 6a and b-iii) corresponds to the depopulation of the ground state, aligning well with the absorption spectra (Fig. 1b). Hence, we assign the initial lifetimes of 0.5 ± 0.1 ps and 0.8 ± 0.1 ps in ACN and DMSO respectively, to the IC and vibrational relaxation from the initially populated $^1\pi\pi^*$ state to the $^1n\pi^*$ state. This assignment is supported by the almost negligible energy difference between the $S_1$ and $S_2$ states in both solvents.

The transient species, reaching its maximum absorption at 425 nm, undergoes decay and a blue shift, while simultaneously absorbing across the visible spectrum. This subsequent decrease in $\Delta A$ is associated with the ISC to a high-energy triplet state. Upon examination of the energy gaps between relevant singlet and triplet states (Table 3), along with the accompanying data on SOC values (Table 4), and considering El-Sayed's rules, it becomes apparent that in DMSO, the ISC to the triplet manifold predominantly occurs *via* a transition from the $S_1(\pi\pi^*)$ state to the $T_2(n\pi^*)$ state, followed by subsequent IC to the $T_1(\pi\pi^*)$ state. In contrast, in ACN, the ISC to the triplet manifold is predicted to occur *via* $S_2(\pi\pi^*) \rightarrow S_1(n\pi^*) \rightarrow T_1(\pi\pi^*)$, involving initial IC from the $^1\pi\pi^*$ to the $^1n\pi^*$ state, followed by ISC from the $^1n\pi^*$ to the $T_1(\pi\pi^*)$ state. Notably, both pathways occur within 3.5 and 10 ps ($\tau_2$) in ACN and DMSO, respectively. Hence, in both solvents, we assign the second lifetime, which is attributed to the red EADS, to ISC to the triplet manifold.

The observed blueshift in transient spectra in both solvents (Fig. 6a and b) is assigned to a combination of vibrational cooling and solvent relaxation dynamics in the triplet manifold occurring within 18 and 106 ps in ACN and DMSO. This assignment is supported by minimal conformational changes

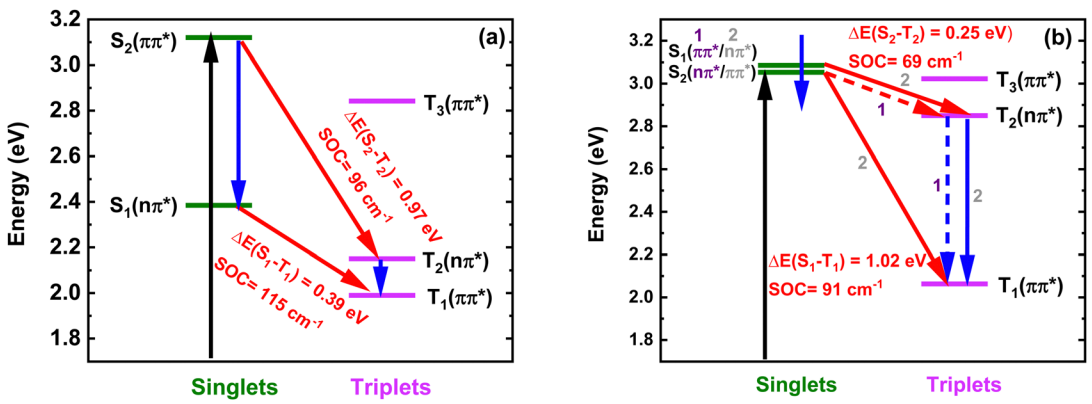


Scheme 2 Proposed deactivation mechanisms for SACD (a) and SCou (b). Red color lines represent ISC while Blue represents IC. In (b), the ISC pathway to the triplet manifold is labeled as "1" in DMSO and depicted with dashed lines, whereas it is labeled as "2" in ACN and shown with solid lines due to the isoenergetic nature of the singlet states and their distinct character in each solvent.

in excited states, where the only noticeable change is the elongation of the carbon–sulfur bond, while the molecule remains planar in both ground and excited states (Fig. 3). Moreover, the variation in $\tau_3$ with solvent, coupled with the significant energy gaps ($\Delta E(S_1–T_1)$ and $\Delta E(S_2–T_1)$) in ACN and DMSO, respectively, further reinforces this assignment, which corresponds to the blue EADS2 in Fig. 7b–d.

The population reaching the triplet state of SCou decays within 10.5 μs in Ar-saturated conditions. The proposed deactivation mechanism of SCou in both solvents is presented in Scheme 2b. Given the isoenergetic nature of the $S_1$ and $S_2$ states and their distinct character changes in different solvents, the ISC pathway to the triplet manifold in DMSO is labeled as ''1'' and depicted with dashed lines, whereas in ACN, it is labeled as ''2'' and shown with solid lines in Scheme 2b.

## Conclusion

We investigated the photophysics and the electronic relaxation pathways of the HAF-PSs SACD and SCou in ACN and DMSO through a combination of steady-state and time-resolved absorption and emission techniques with time scales ranging from femtosecond to microseconds. The experimental work was complemented with ground and excited state calculations at the TD-DFT level of theory. The comprehensive investigation provided experimental and computational evidence elucidating the excited states responsible for the near unity nonradiative decay in these molecules. Specifically, it was demonstrated that both SACD and SCou exhibit excellent photophysical properties as HAF-PSs, including high absorption in the visible, ultrafast ISC and near unity triplet yields, and long-lived triplet states decaying in *ca.* 3 and 11 microseconds under Ar-saturated conditions. In addition, SACD and SCou showed high bimolecular triplet quenching constants by $O_2$, and high singlet oxygen quantum yields of 93% and 43%, respectively. The significance of long-lived triplet states and singlet oxygen generation by both molecules lies in their ability to elicit cancer cell death. Collectively, the findings underscore the versatility of SACD and SCou for applications in photodynamic therapy, as well as, for other diverse applications across various fields, including photon upconversion, photovoltaics, and photocatalysis.

## Author contributions

C. A.: investigation, formal analysis, writing – original draft, writing review, and editing. S. H.: investigation, formal analysis, writing review, and editing. S. K.: investigation, writing review, and editing. S. Y.: investigation, writing review, and editing. S. K. S.: investigation, writing review, and editing. E. L.: investigation, writing review, and editing. S. J.: investigation, writing review, and editing. H. X.: investigation, writing review, and editing. C. E. C.-H.: conceived the study, funding acquisition, project administration, resources, supervision, visualization, validation, writing – review, and editing.

## Data availability

Experimental and computational procedures and all relevant data are available in the ESI,† and from the authors upon reasonable request.

## Conflicts of interest

There are no conflicts to declare.

## Acknowledgements

The authors acknowledge funding from the National Science Foundation (grant no. CHE-2246805), National Institute of General Medical Sciences (R35-GM133706), and the Robert A. Welch Foundation (C-1970). The authors also acknowledge Case Western Research University Expanding Horizons Initiative in the College of Arts and Sciences through a 2023 Interdisciplinary award (INT-L) and the High-Performance Computing Resource in the Core Facility for Advanced Research Computing at Case Western Reserve University.

## Notes and references

1 L. A. Ortiz-Rodríguez and C. E. Crespo-Hernández, *Chem. Sci.*, 2020, **11**, 11113–11123.
2 V. N. Nguyen, Y. Yan, J. Zhao and J. Yoon, *Acc. Chem. Res.*, 2020, **54**, 207–220.
3 J. Tang, L. Wang, A. Loredo, C. Cole and H. Xiao, *Chem. Sci.*, 2020, **11**, 6701–6708.
4 B. Ashwood, M. Pollum and C. E. Crespo-Hernández, *Photochem. Photobiol.*, 2019, **95**, 33–58.
5 M. Pollum, L. Guan, S. Ahsanuddin, E. Baron, M. Lam and C. E. Crespo-Hernández, *J. Invest. Dermatol.*, 2016, **136**, S105.
6 M. Pollum, M. Lam, S. Jockusch and C. E. Crespo-Hernández, *ChemMedChem*, 2018, **13**, 1044–1050.
7 X. Luo, Y. Yang and X. Qian, *Chin. Chem. Lett.*, 2020, **31**, 2877–2883.
8 V. N. Nguyen, S. Qi, S. Kim, N. Kwon, G. Kim, Y. Yim, S. Park and J. Yoon, *J. Am. Chem. Soc.*, 2019, **141**, 16243–16248.
9 Y. Bo, H. Zhang, Y. Li, Y. Reva, L. Xie and D. M. Guldi, *Angew. Chem., Int. Ed.*, 2024, **136**, e202313936.
10 G. Turkoglu, G. K. Koygun, M. N. Z. Yurt, N. Demirok and S. Erbas-Cakmak, *Org. Biomol. Chem.*, 2020, **18**, 9433–9437.
11 A. A. Buglak, A. Charisiadis, A. Sheehan, C. J. Kingsbury, M. O. Senge and M. A. Filatov, *Chem. – Eur. J.*, 2021, **27**, 9934–9947.
12 P. P. P. Kumar, P. Yadav, A. Shanavas, S. Thurakkal, J. Joseph and P. P. Neelakandan, *Chem. Commun.*, 2019, **55**, 5623–5626.
13 J. Tang, M. A. Robichaux, K.-L. Wu, J. Pei, N. T. Nguyen, Y. Zhou, T. G. Wensel and H. Xiao, *J. Am. Chem. Soc.*, 2019, **141**, 14699–14706.
14 L. A. Ortiz-Rodríguez, S. J. Hoehn, A. Loredo, L. Wang, H. Xiao and C. E. Crespo-Hernández, *J. Am. Chem. Soc.*, 2021, **143**, 2676–2681.

15 S. Jena, K. D. Tulsiyan, A. Kumari, R. Das and H. S. Biswal, *J. Phys. Chem. B*, 2022, **126**, 6083–6094.
16 W. Hu, R. Zhang, X. F. Zhang, J. Liu and L. Luo, *Spectrochim. Acta, Part A*, 2022, **272**, 120965.
17 V. N. Nguyen, J. Ha, M. Cho, H. Li, K. M. K. Swamy and J. Yoon, *Coord. Chem. Rev.*, 2021, **439**, 213936.
18 J. Piskorz, W. Porolnik, M. Kucinska, J. Dlugaszewska, M. Murias and J. Mielcarek, *ChemMedChem*, 2021, **16**, 399–411.
19 M. Pollum, L. Martínez-Fernández and C. E. Crespo-Hernández, *Photoinduced Phenomena in Nucleic Acids I*, ed. M. Barbatti, A. C. Borin and S. Ullrich, Springer, Cham, Switzerland, 2015, vol. 355, pp. 245–327.
20 M. M. Brister, T. Gustavsson and C. E. Crespo-Hernández, *Molecules*, 2020, **25**, 584.
21 B. Ashwood, S. Jockusch and C. E. Crespo-Hernández, *Molecules*, 2017, **22**, 379.
22 C. Reichardt, C. Guo and C. E. Crespo-Hernández, *J. Phys. Chem. B*, 2011, **115**, 3263–3270.
23 S. Mai, M. Pollum, L. Martínez-Fernandez, N. Dunn, P. Marquetand, I. Corral, C. E. Crespo-Hernández and L. Gonzalez, *Nat. Commun.*, 2016, **7**, 1–8.
24 U. Mayer, V. Gutmann and V. W. Gerger, *Monatsh. Chem.*, 1975, **106**, 1235–1257.
25 A. D. Becke, *J. Chem. Phys.*, 1993, **98**, 1372–1377.
26 C. Adamo and V. Barone, *J. Chem. Phys.*, 1999, **110**, 6158–6170.
27 T. Yanai, D. P. Tew and N. C. Handy, *Chem. Phys. Lett.*, 2004, **393**, 51–57.
28 X. Xu and W. A. Goddard, *Proc. Natl. Acad. Sci. U. S. A.*, 2004, **101**, 2673–2677.
29 M. A. El-Sayed, *J. Chem. Phys.*, 1963, **38**, 2834–2838.
30 A. D. Laurent and D. Jacquemin, *Int. J. Quantum Chem.*, 2013, **113**, 2019–2039.